Vibration phases estimation based on orthogonal interferometry of inner view field for ISAL imaging and detection

Kai Zhou,[1,2] **Daojing Li,**[1,*] **Jinghan Gao,**[1,2] **Anjing Cui,**[1,2] **Jiang Wu,**[1,2] **Shumei Wu,**[1] **Yefei Wang,**[3] **Kai Liu,**[3] **Songnian Tan,**[3] **Yang Gao,**[3] **and Yuan Yao**[3]

[1]*National Key Laboratory of Microwave Imaging Technology, Aerospace Information Research Institute of Chinese Academy of Sciences, Beijing 100190, China*
[2]*School of Electronic, Electrical and Communication Engineering, University of Chinese Academy of Sciences, Beijing 100049, China*
[3]*Changchun Institute of Optics, Fine Mechanics and Physics, Chinese Academy of Sciences, Changchun 130033, China*
*lidj@mail.ie.ac.cn

Inverse synthetic aperture ladar (ISAL) has the capability to achieve high-resolution imaging of long-distance targets in a short time because of the laser's short wavelength. However, the unexpected phases introduced by target vibration in the echo can cause defocused imaging results of the ISAL. How to estimate the vibration phases has always been one of the difficulties in ISAL imaging. In this paper, in view of the echo's low signal-to-noise ratio, the orthogonal interferometry method based on time-frequency analysis is proposed to estimate and compensate the vibration phases of ISAL. The method can effectively suppress the influence of noise on the interferometric phases and accurately estimate vibration phases using multichannel interferometry in the inner view field. The effectiveness of the proposed method is validated through simulations and experiments, including a 1200 m distance cooperative vehicle experiment and a 250 m distance noncooperative unmanned aerial vehicle experiment.   © 2023 Optica Publishing Group

1. INTRODUCTION

Based on the improvement of the laser coherence, inverse synthetic aperture radar (ISAR) technology can be applied in the laser waveband, known as inverse synthetic aperture ladar (ISAL). It achieves high range resolution through pulse compression of a broadband laser signal and high cross-range resolution through synthetic aperture technology [1].

Because ISAL operates in the optical band, its wavelength is shorter by at least three orders than that of microwaves, which gives ISAL the ability to achieve high-resolution imaging of targets in a short time [2,3], play an important role in the military field [4], and make ISAL a research hotspot [5–9]. In addition, based on ISAL's beam expansion and the transmitting-receiving reciprocity principle [10], a wide receiving field of view (FOV) can be achieved using only a small number of detectors [11], thereby greatly reducing the complexity of the optical system and the amount of ladar data. However, ISAL is sensitive to target vibration due to its micrometer magnitude wavelength. Even a vibration of micrometer magnitude can introduce unexpected phases (hereinafter referred to as the vibration phases) in the echo, causing the imaging results to be defocused. Therefore, the estimation and compensation of the vibration phases are of great significance for ISAL imaging [12,13].

The phase gradient autofocus (PGA) and the space correlation algorithm (SCA) [14] are used to estimate target vibration phases in ISAL imaging; however, they are dependent on the target characteristics, which limit their robustness. In contrast, multichannel interferometry can estimate the target vibration phases without depending on the target characteristics, resulting in higher estimation accuracy and more accurate imaging results. In [15,16], a method based on three-channel orthogonal baseline interferometry processing is proposed to estimate and compensate the vibration phases, but they have only been verified by simulations. In [17], the method based on dual-channel interferometry of ISAL outer FOV is proposed to estimate the vibration phases of a target with 70 m distance. However, if the aperture of the receiving optical system is to be increased to obtain the echo of a longer distance target, the complexity of the system and interferometry baseline will be greatly increased, and the estimation accuracy of the interferometry will drop. In [18], the system scheme, index parameters, and key technologies of one transmitting and four receiving ladar systems are analyzed, which shows the advantages in imaging and detection of system. In addition to being more flexible in the form of orthogonal interferometry of four channels, it is similar to a four-quadrant detector, which can also obtain azimuth/pitch

angle information of the target through amplitude/phase ratio processing.

Based on [18], in this paper, the experiment system and observation geometry of the ISAL are introduced in Section 2. Then, in view of the low signal-to-noise ratio (SNR) of the echo, the multichannel orthogonal interferometry method based on time-frequency analysis is proposed to estimate and compensate the vibration phases of ISAL. In Section 3, the principle of the proposed method is explained. Finally, in Section 4, the simulations and experiments of the cooperative vehicle at about 1200 m away and the noncooperative unmanned aerial vehicle (UAV) at about 250 m away are carried out to verify the effectiveness and accuracy of the proposed method.

2. EXPERIMENT SYSTEM

The coherent ladar consists of transmitting and receiving optical telescopes, a narrow pulse laser, five laser local oscillator balanced detectors, a transmitter, a signal generation, and analog-to-digital (AD) conversion module [10]. The system schematic diagram is shown in Fig. 1.

Two points need to be noted in Fig. 1. First, after the laser signal is transmitted by the telescope, a coupling lens is used to obtain the transmitting reference signal and record the unexpected time-varying phases in the laser signal, and the phase error of laser echo signal is removed by transmitting reference correction before subsequent imaging processing. Second, the real signals are obtained by single-channel sampling; then, the complex signals are constructed by the fast-time Hilbert transform.

The positional relationship between the transmitting telescope and receiving telescope of the ladar is shown in Fig. 2. The ladar adopts the transmitter–receiver separation mode and uses the collimator to adjust the direction of the transmitting beam to align with receiving FOV at the far-field target. In order to form four receiving channels, four fiber collimators labeled as T_1, T_2, $\cdots$ T_4 are set on the inner FOV of one large receiving telescope [16,18,19], which are placed symmetrically in pairs, and the inner FOV system can ensure a short baseline while ensuring sufficient SNR through a large aperture (0.6 mm baseline length and 100 mm aperture in this article). In order to increase the observation swath and form overlapping FOV for vibration phases estimation by interferometry, a second-order phase cylindrical lens is added to the transmitting telescope to the expanding beam in the pitch direction [10], and the fiber collimators with high-order phaser are set in receiving telescope to introduce a wide FOV laser signal into the fiber without having an impact on coupling efficiency [11,18,19]. As the transmitting telescope is located at T, the equivalent
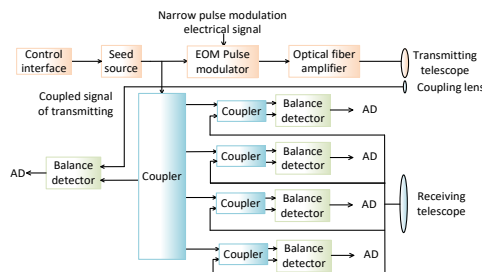

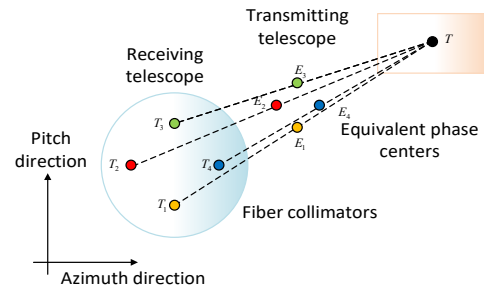**Fig. 2.** Schematic diagram of the layout of one transmitting and four receiving in inner FOV.

phase centers, labeled E_1, E_2, $\cdots$ E_4, are at the middle points between the fiber collimators and the phase center of the transmitting telescope. For the convenience of analysis, "channel" is used instead of "equivalent phase center" for description in the following. Based on the analysis of [10], the coherence between channels has been guaranteed, and the remaining system parameters of the ladar are the same as in [18].

3. METHOD

A. Orthogonal Interferometry by Four Channels of Inner FOV

Figure 3 presents the orthogonal interferometry by the four channels (OI4C) method of squint ISAL, in which the global coordinate system is the coordinate system XYZ, and the vehicle target moves in the opposite direction of Y axis at a velocity $\vec{V}$. When it passes through the laser beam, the corresponding positions in the XOY plane are X_c and Y_c, where θ and ϕ are the ladar squint angle and pitch angle (downward is positive), respectively.

The transmitter and receiver are located at the height H, and their local coordinate system is defined as $X'Y'Z'$, in which the X' axis is the direction of the ladar line of sight. The Y' axis is parallel to the XOY plane and perpendicular to the X' axis, the angle between the Y' and Y axes is the squint angle θ, and the Z' axis is perpendicular to the X' and Y' axes, simultaneously. The echo signal of the target can be received by channel E_1, E_2, E_3, E_4 when the target moves to position P_1, P_2, P_3, P_4 at time t_{k1}, t_{k2}, t_{k3}, t_{k4}, which can be expressed as follows (the artificial correspondence between the target position subscripts and the channel subscripts is for the simplicity of the subsequent formula):
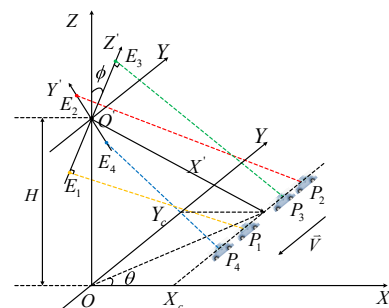

Fig. 1. System schematic diagram.

Fig. 3. Orthogonal interferometry model by four channels of squint ISAL.

$$s_a(\hat{t}, t_{ka}) = \sigma \cdot p(\hat{t} - 2 \cdot R_a(t_{ka})/C) \cdot \exp\left(-j \cdot \frac{4\pi \cdot R_d(t_{ka})}{\lambda}\right) \cdot \exp\{j \cdot \varphi_v(t_{ka})\}, \tag{1}$$

where a represents the channel order; σ represents the reflection coefficient of the scattering point; $\hat{t}$ and t_{ka} represent the fast time and slow time, respectively; C represents the light speed; λ represents the wavelength of the laser; a represents the channel number; $R_a(t_{ka})$ represents the range between E_a and P_a at t_{ka}; $p(\hat{t})$ represents the narrow pulse signal corrected by the transmitting reference; and $\varphi_v(t_k)$ represents the vibration phases introduced by the target. Subsequently, interferometry between $s_2(\hat{t}, t_{k2})$ and $s_4(\hat{t}, t_{k4})$, $s_1(\hat{t}, t_{k1})$ and $s_3(\hat{t}, t_{k3})$ are applied after registration, respectively, and the interferometric phases can be expressed as (since the interferometry needs to be completed in the overlapping FOV of channels, at this time $P_1 \sim P_4$ can be equivalent to the one position)

$$\begin{cases} \Delta\varphi_{24}(t_k) = -\frac{4\pi}{\lambda} \cdot (R_2(t_{k2}) - R_4(t_{k4})) + \varphi_v(t_{k2}) - \varphi_v(t_{k4}) \\ \Delta\varphi_{13}(t_k) = -\frac{4\pi}{\lambda} \cdot (R_1(t_{k2}) - R_3(t_{k4})) + \varphi_v(t_{k1}) - \varphi_v(t_{k3}) \end{cases}. \tag{2}$$

Due to the existence of the squint angle, the range of the targets observed at different time by different receiving channels are different, and the phases $-\frac{4\pi}{\lambda} \cdot (R_2(t_{k2}) - R_4(t_{k4}))$ caused by the range change also exist in the interferometric phases. At this time, the differential values $\varphi_v(t_{k2}) - \varphi_v(t_{k4})$ of the vibration phases cannot be directly extracted from the interferometric phases. Under this circumstance, it is necessary to use the interferometric phases of the two orthogonal baselines to remove the phases introduced by the range change with the target motion parameters and the observation geometry. Subsequently, the differential values of the vibration phases can be obtained to calculate the gradients, and the estimated vibration phases can be obtained by the integration of the gradients as

$$\varphi_v(t_k)' = \int_0^{t_k} \nabla\varphi_v(T)\mathrm{d}T = \varphi_v(t_k) - \varphi(0), \tag{3}$$

where $\nabla\varphi_v(t_k)$ is the gradient of the vibration phases at slow time t_k, based on the references [15,16], the calculation formula of the gradient of vibration phases can be expressed as follows:

$$\nabla\varphi_v(t_k) = \|\vec{V}\| \cdot \frac{\Delta\varphi_{24}(t_k) \cdot (L_{13}\cos(\theta)\sin(\theta)) + \Delta\varphi_{13}(t_k) \cdot (L_{24}\sin(\phi))}{-2L_{24} \cdot L_{13}\sin(\theta)} + \|\vec{V}\| \cdot \frac{4\pi}{-2\lambda}(\sin(\theta) \cdot \cos(\phi))$$

$$+ \|\vec{V}\| \cdot \frac{\sin(\phi)}{-2\sin(\theta)} \cdot \frac{4\pi}{\lambda}\left(-\sqrt{\frac{\sin(\theta)^2}{\tan(\phi)^2} + \cos(\theta)^2} \cdot \cos\left[\begin{array}{c}\arccos\left(-\frac{\cos(\theta) \cdot \sin(\phi)}{\sqrt{\sin(\theta)^2/\tan(\phi)^2 + \cos(\theta)^2}}\right) \\ + \arccos(\cos(\phi) \cdot \cos(\theta))\end{array}\right]\right), \tag{4}$$

where L_{24} and L_{13} are the baseline lengths between Channel 2 and Channel 4, Channel 1 and Channel 3, respectively.

B. Noise Reduction by Interferometry in Time-Frequency Domain

Estimation accuracy of the OI4C method is greatly affected by the SNR of the target echo signal; however, the noise in the actual data is inevitable. In order to effectively suppress the noise, based on the time-frequency analysis of the slow time

dimension of the echo signal, it is proposed to perform interferometry processing in the time-frequency domain in this paper, which realizes coherent accumulation of multiple pulses by using the Fourier transform and maintains the coherence of the signal. Theoretically, the coherent accumulation of M pulses can increase the SNR by M times.

Let the time-frequency analysis of a range cell of the echo signal $s_a (a \in [1, 4])$ be s_{a_stft} (the overlap size of the time-frequency analysis is 1 less than the window size) and n, m represent the number of Doppler frequency points and number of slow time points of the time-frequency analysis s_{a_stft}, respectively. In order to effectively extract the interferometric phases, the coherence coefficient matrices $\gamma_{24}(n, m)$ and $\gamma_{13}(n, m)$ are obtained from the time-frequency analysis of Channel 2 and Channel 4, Channel 1 and Channel 3, respectively, and can be expressed by the following formula:

$$\gamma_{24}(n_c, m_c) = \rho(s_{2\_stft}(n_l, m_l), s_{4\_stft}(n_l, m_l))$$

$$\gamma_{13}(n_c, m_c) = \rho(s_{1\_stft}(n_l, m_l), s_{3\_stft}(n_l, m_l))$$

$$n_l = [n_c - l/2, n_c + l/2], \quad m_l = [m_c - l/2, m_c + l/2]$$

$$n_c \in [l/2 + 1, n - l/2], \quad m_c \in [l/2 + 1, m - l/2], \tag{5}$$

where $\rho(\cdot)$ represents the correlation coefficient of two matrices, l represents the length of the neighborhood used, which is generally much shorter than the length of the original matrix. By filling zeros at the boundary, $\gamma_{24}(n, m)$ and $\gamma_{13}(n, m)$ with the same size of the original matrix can be obtained. As an example, the coherence coefficient diagrams in Figs. 7(a) and 7(b) are the coherence coefficient matrices of the echo in the time domain and time-frequency domain.

Thereby the threshold matrices $W_{24}(n, m)$ and $W_{13}(n, m)$ can be constructed by setting appropriate coherence coefficient thresholds th_{24} and th_{13} to effectively extract the interferometric phases

$$W_{24}(n, m) = \left[\gamma_{24}(n, m) \underset{1}{\overset{0}{\lessgtr}} th_{24}\right],$$

$$W_{13}(n, m) = \left[\gamma_{13}(n, m) \underset{1}{\overset{0}{\lessgtr}} th_{13}\right], \tag{6}$$

$$\begin{cases} \Delta\varphi_{24}(t_k) = \text{angle}\left[\sum_{n=N_{\min}}^{n=N_{\max}} s_{2\_stft}(n, m) \cdot s_{4\_stft}^*(n, m) \cdot W_{24}(n, m)\right] \\ \Delta\varphi_{13}(t_k) = \text{angle}\left[\sum_{n=N_{\min}}^{n=N_{\max}} s_{1\_stft}(n, m) \cdot s_{3\_stft}^*(n, m) \cdot W_{13}(n, m)\right] \end{cases}, \quad (7)$$

where $N_{\min}$ and $N_{\max}$ are the minimum and maximum values of the instantaneous Doppler frequency in the time-frequency analysis of the gated interferometric phases, respectively. When the selected threshold is high, the gated interferometric phases correspond to the high energy frequency range of the signal in the time-frequency domain, and the noise can be further reduced by accumulating the interferometric phases in this range. Finally, the above operations are performed on the rest of the range cells of the echo; then, the vibration phases estimation accuracy can be further improved by coherent accumulation of multiple range cells.

Figure 4 depicts the flowchart of the vibration phases estimation by the OI4C method of ISAL imaging. Among them, the "preprocessing" step includes four steps: fast-time Hilbert transform; transmitting reference correction; bandpass filtering and denoising; and registration. Additionally, the "target parameter estimation" step includes estimation of the slow time-frequency modulation and the cross-range velocity of the target, and the "coarse compensation" refers to the coarse compensation for the time-varying Doppler center caused by the squint angle, target distribution, and velocity component in elevation. After the interferometry of four channels are applied in the time-frequency domain, the vibration phases can be estimated by the OI4C method. Finally, the range Doppler (RD) algorithm is used as the ISAL imaging algorithm [20] to obtain the imaging result after vibration phases compensation.

Two more points need to be noted about the OI4C method. First, the magnitude of velocity $\vec{V}$ of the target should be estimated before the OI4C method is used. Further, the range velocity and cross-range velocity of the target can be estimated through the Doppler center and slow time-frequency modulation, respectively [21], so the magnitude of velocity $\vec{V}$ can be obtained. Second, the window size needs to be selected when performing time-frequency analysis on the echo signal. Although increasing the window size can improve the SNR
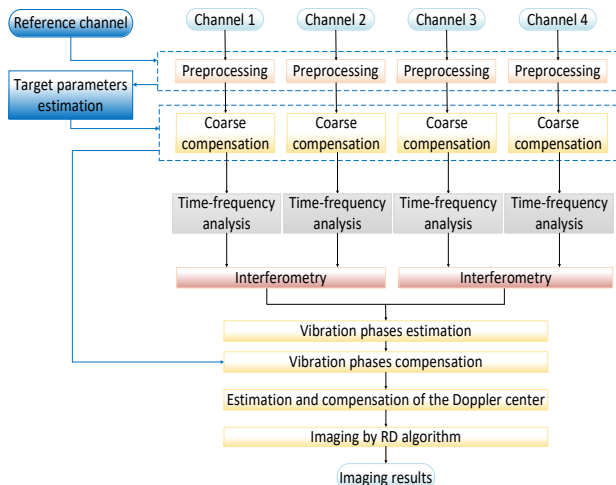
when the noise in echo is great, the window size should not be too large. The selection principle is that the vibration phases should change almost linearly within the window. In this case, the phase errors caused by the remaining pulses in the window are small, which can reduce estimation errors of the vibration phases.

4. SIMULATION AND EXPERIMENT

In this section, simulation and ISAL experiments are carried out to verify the effectiveness and accuracy of the proposed method. Section 4.A presents the simulation analysis, Section 4.B presents the cooperative vehicle and noncooperative UAV experiments, and Section 4.C discusses the applicability of the OI4C method.

A. Simulation

The simulation parameters are shown in Table 1. The target scene contains a vehicle and a single scattering point, as shown in Fig. 5. The setting of a single scattering point is helpful for checking the compensation effect of vibration phases.

The echo in the time-domain and time-frequency analysis of the thirty-fifth range cell of the echo with and without coarse

Table 1.   ISAL System Parameters in Simulation

Parameters	Values
Wavelength	1550 nm
Transmitting signal pulse width	5 ns
Sampling rate	4 GHz
PRF	100 kHz
Pitch/azimuth beamwidth	3/0.1 mrad
Range	1214 m
Squint/pitch angle	6.2°/2.4°
Range/cross-range velocity	1.05 m/s/9.95 m/s
Doppler center frequency	1.34 MHz
Slow time-frequency modulation	105 kHz/s
Cross-range imaging filter band	2.6 kHz
Range/cross-range resolution	0.75 m/better than 1 cm
Vibration amplitude/frequency	10 μm/30 Hz
Doppler band vibration-caused	5 kHz

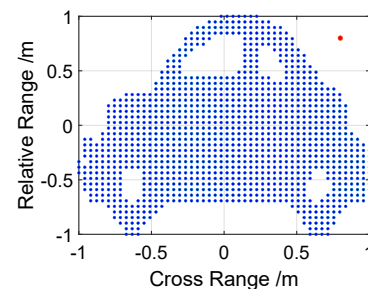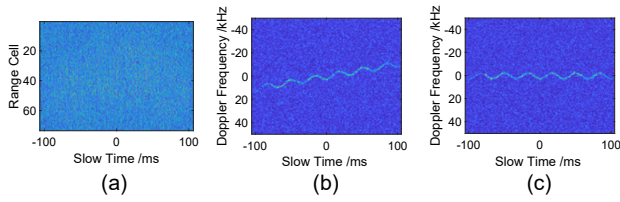**Fig. 4.**   Signal processing flowchart of OI4C method.


Fig. 5.   Target in simulation.

Fig. 6. Echo in the time domain; time-frequency analysis of the thirty-fifth range cell of the echo with and without the coarse compensation. (a) Echo in the time domain. (b) Time-frequency analysis without the coarse compensation. (c) Time-frequency analysis with the coarse compensation.
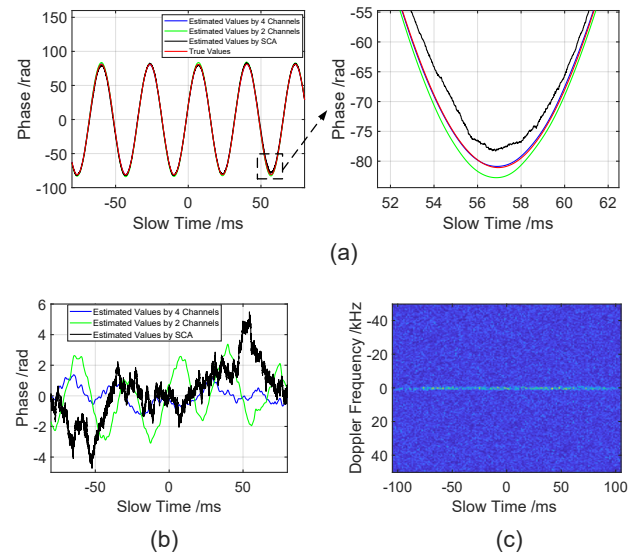
compensation (time-frequency analysis with 256 window length and 255 overlap) are shown in Fig. 6. The single-pulse SNR in the echo is about −3 dB; obviously, the SNR of the time-frequency domain is higher.

To better illustrate the difference between the signal coherence in the time domain and time-frequency domain, Fig. 7 shows the coherence coefficient diagram, the histogram, and the interferometric phase diagram of the two-channel signal (taking interferometry between Channel 2 and Channel 4 as an example, consistent with subsequent two-channel interferometry) in the time domain and time-frequency domain, respectively. For a fair comparison, the coherence coefficient histograms are both drawn using the coherence coefficients from the thirtieth to fortieth range cell in these two domains. Moreover, the interferometric phase diagram is gated to display the target area by using the echo without noise. Obviously, it can be seen that the coherence coefficients in the time domain are mainly distributed in the range of 0.1–0.4, which are affected by noise. By contrast, the coherence coefficients in the time-frequency domain are mainly distributed above 0.8, the coherence is higher, and the interferometric phases are less affected by noise.

The estimation of vibration phases is performed using SCA, interferometry between Channel 2 and Channel 4 (I2C method) and OI4C method, respectively. Estimation results and estimation errors are shown in the black, green, and blue curves in Figs. 8(a) and 8(b). Meanwhile, the true values of the added vibration phases are represented by the red curve, and the time-frequency analysis after compensation by the OI4C method is shown in Fig. 8(c). In additional, the root mean
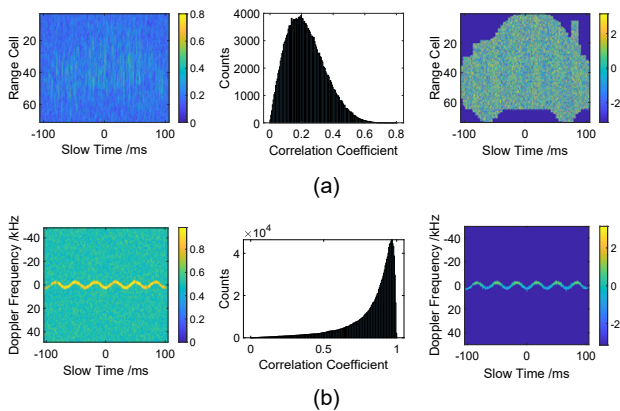
Fig. 7. Coherence coefficient diagram, histogram and interferometric phase diagram of the two-channel signal in the (a) time domain and (b) time-frequency domain.


Fig. 8. True values, estimated values, estimated errors of vibration phases, and time-frequency analysis after compensation by OI4C method. (a) True values and estimated values of vibration phases. (b) Estimation errors. (c) Time-frequency analysis after compensation by OI4C method.

square error (RMSE) of the estimated values is calculated, which are 3.6, 2.4, and 0.9 rad in turn (the mean of 50 Monte Carlo simulations), corresponding to SCA and the I2C and OI4C methods. Obviously, it can be seen that the estimated values of the OI4C method are closest to the true values of the vibration phases; after compensation, the Doppler band is narrowed and the vibration phases are removed. Due to the existence of the squint angle, the residual phase errors of the I2C method are a bit large, and the estimation errors of SCA are also a bit large, additionally.

After compensation by using the above estimated values, Figs. 9(b)–9(d) present the imaging results, cross-range slices, and enlarged images, respectively. For reference, Figs. 9(a) and 9(e) show the imaging results without and with phase compensation by using the true values, simultaneously. (In order to compare the imaging results of the single scatter point with different compensation method clearly, the enlarged images in the third column are renormalized by the maximum value in the red box of the second column.)

Obviously, it can be seen that the imaging result without compensation is seriously defocused from Fig. 9(a), and the single scattering point cannot be identified. After the compensation by the OI4C method, the focusing degree is significantly improved, which is the closest to the imaging result with compensation by the true values, and the SNR of the imaging result is about 25 dB. However, after compensation by using the I2C method and SCA, the main and side lobes of the single scattering point have different degrees of broadening and rising, respectively.

To further demonstrate the effectiveness of the OI4C method, the image entropy and image contrast are used to quantitatively describe the focusing degree of the imaging results. The formulas are as follows:
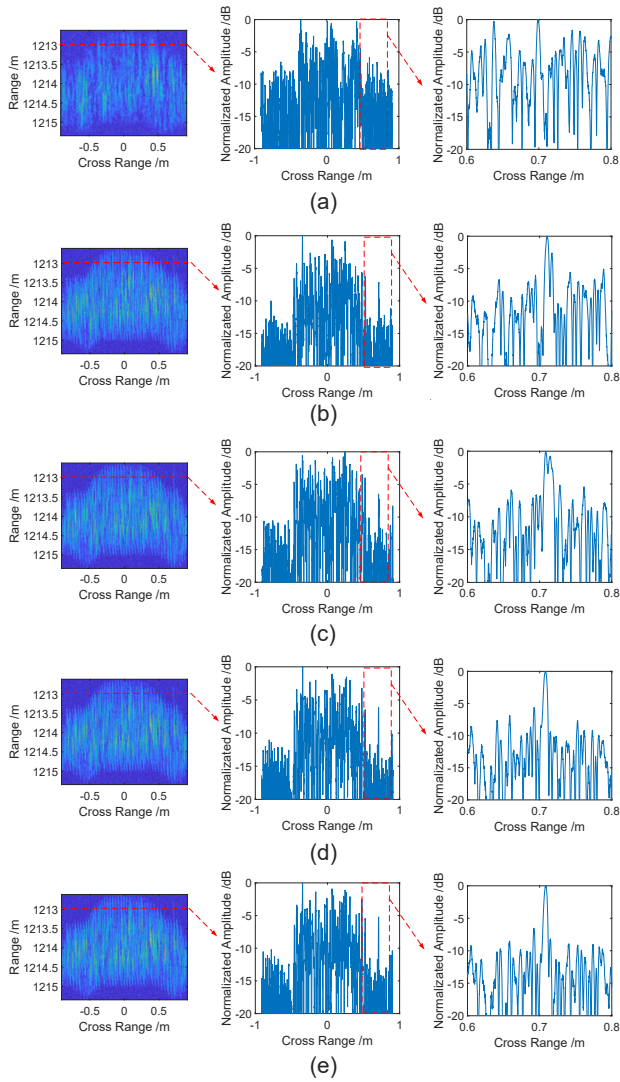
Fig. 9. Imaging results with and without the compensation by different method. (a) Without compensation. (b) Compensation with SCA. (c) Compensation with I2C method. (d) Compensation with OI4C method. (e) Compensation with true values.

$$\begin{cases} H(I) = -\sum_{j=1}^{J} \sum_{k=1}^{K} p(j,k) \cdot \ln p(j,k) \\ C(I) = \frac{1}{u} \sqrt{\frac{1}{JK} \cdot \sum_{j=1}^{J} \sum_{k=1}^{K} (|I(j,k)| - u)^2} \end{cases}, \quad (8)$$

where $p(j,k) = |I(j,k)|^2 / (\sum_{j=1}^{J} \sum_{k=1}^{K} |I(j,k)|^2)$ presents the power normalized image, $I(j,k)$ presents the complex imaging result, $u = \sum_{j=1}^{J} \sum_{k=1}^{K} |I(j,k)| / (JK)$ presents the average intensity of the image, and J and K present the 2D pixel points of the image, respectively. The focusing degree is better with less image entropy and greater image contrast.

After calculation, Table 2 shows the evaluation indexes of the results in Fig. 9. It can be seen that the focusing degree of the imaging result with the compensation by the OI4C method is the closest to the ideal situation, while there is still some degree of defocusing of the imaging results with the compensation by the I2C method and SCA.

Table 2. Evaluation Index of Simulation Imaging Results

| Parameters	Fig. 9(a)	Fig. 9(b)	Fig. 9(c)	Fig. 9(d)	Fig. 9(e)
Entropy	9.22	8.35	8.29	8.03	7.98
Contrast	0.65	1.27	1.33	1.52	1.56
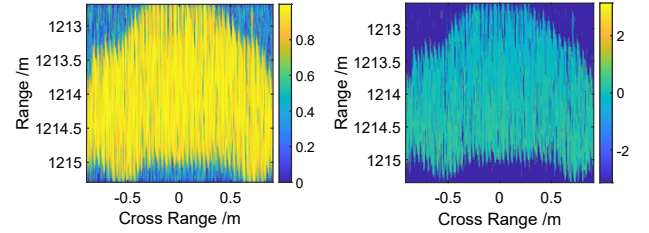
Fig. 10. Coherence coefficient images and the interferometric phase images of the imaging results of Channel 2 and Channel 4 after compensation by OI4C method.

Furthermore, the coherence coefficient images and the interferometric phase images (gated by using the coherence coefficient images) of the imaging results of Channel 2 and Channel 4 after compensation by OI4C method are shown in Fig. 10. Most of the coherence coefficients in the target area are above 0.85, and the interferometric phases are stable after compensation, which indicates the effectiveness of the OI4C method.

The influence of SNR and domain of interferometry on the estimation accuracy of the OI4C method is analyzed below. Figure 11 shows the RMSE of the estimated values under different SNR levels and domains of interferometry. To avoid randomness, 50 Monte Carlo simulations are carried out, and the average of the 50 simulations is shown. Three conclusions can be drawn from Fig. 11. First, in the case of high SNR, the RMSE with time-domain interferometry is slightly lower than the RMSE with time-frequency domain interferometry. Second, in the case of low SNR, the RMSE with time-frequency domain interferometry is significantly lower than the RMSE with time-domain interferometry. Third, whatever the interferometry in the time domain or in the time-frequency domain, the RMSE of the OI4C method decreases with the increase of the echo SNR.

B. Experiments

In this section, the ISAL experiments of 1200 m away cooperative vehicle and 250 m away noncooperative UAV are carried out to validate the effectiveness of the proposed method.
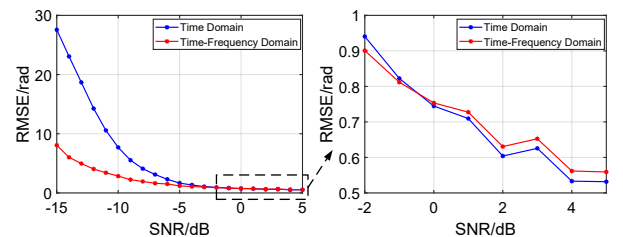
Fig. 11. RMSE of the estimated values with different interferometry domain under different SNR.

1. Cooperative Vehicle Experiment

For the cooperative vehicle, there are four high-reflectivity strips affixed in the horizontal direction of the vehicle, and the layout intervals are 70.5, 5, and 124.5 cm. The observation geometry is shown in Fig. 3; a photo of the vehicle is shown in Fig. 12. The cross-range velocity of the target is estimated to be about 10.6 m/s; the remaining experimental parameters are consistent with those shown in Table 1.

Figure 13 illustrates the echo signal after coarse compensation, the coherence coefficient images, and the interferometric phase curve of the first high-reflectivity strip echo of two channels in the time domain and time-frequency domain. It needs to be noted that the echo in the time domain here has been denoised by bandpass filtering in the slow time dimension (the echoes in time domain shown in the following are all first processed by this operation); otherwise, the signal cannot be identified in the time domain. In this case, the coherence coefficient images are gated by the echo signal greater than 10 dB/13 dB in the time domain/time-frequency domain, respectively. It can be seen that, after the transformation from the time domain to the time-frequency domain, most of the coherence coefficients in the signal region are increased from 0.5 to 0.7, and the interferometric phases are less affected by noise, which can reduce the estimation errors of the vibration phases.

The estimation of vibration phases is carried out by using SCA and the I2C and OI4C methods, respectively. The estimation results and the time-frequency analysis after compensation by the OI4C method of the first high-reflectivity strip are shown

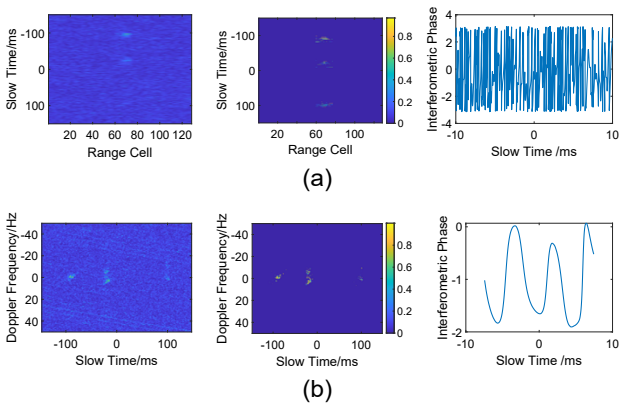**Fig. 12.** Photo of cooperative vehicle.

Fig. 13. Echo signal, the coherence coefficient images, and the interferometric phase curve in (a) time domain and (b) time-frequency domain.
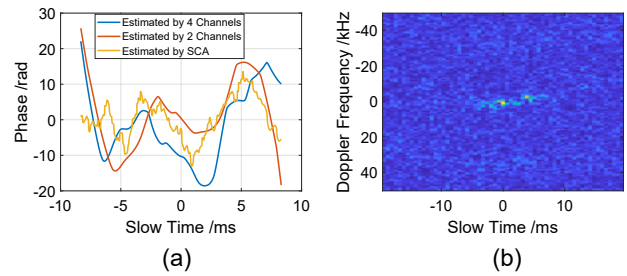

Fig. 14. (a) Estimated values of vibration phases and (b) time-frequency analysis after compensation by OI4C method.

in Fig. 14. Figure 15 shows the imaging results, cross-range slices, and enlarged images with and without the compensation by using the above estimation results, respectively. It can be seen that the imaging result without compensation is seriously defocused, while, after the compensation by the OI4C method, the focusing degree of the imaging result has been significantly improved. Further, the image entropy decreases from 10.5 to 9.2, and the image contrast increases from 0.72 to 0.88. Meanwhile, the two high-reflectivity strips separated by 5 cm in the middle of the vehicle are well distinguished, indicating that the cross-range resolution is better than 5 cm. Assuming the target moves at a uniform velocity within the echo time, it can be calculated that the intervals of four high-reflectivity strips are
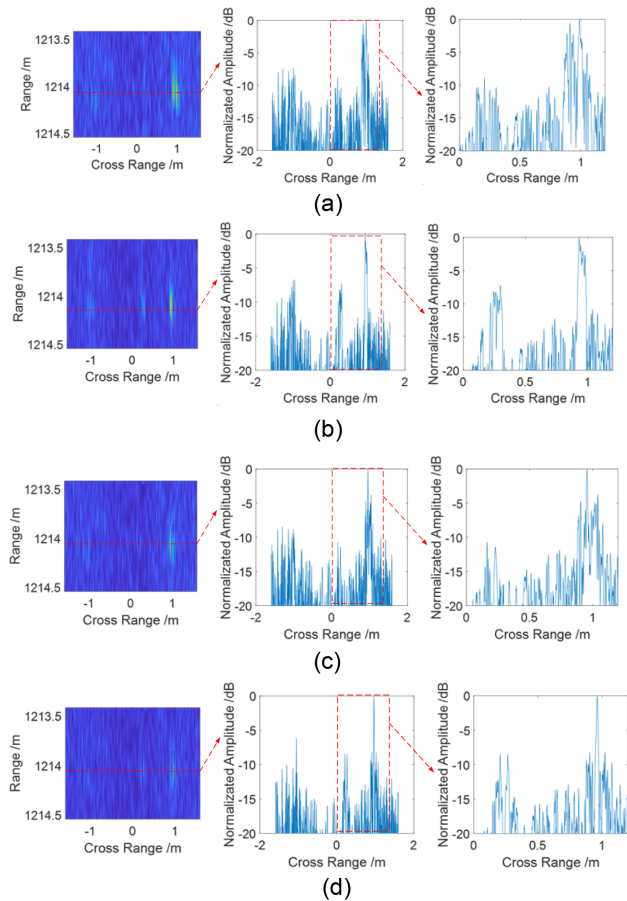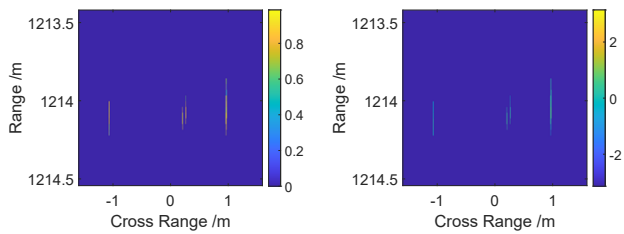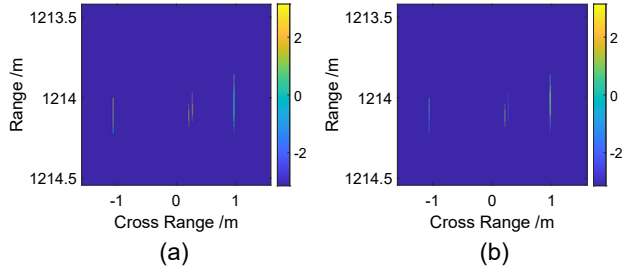

Fig. 15. Imaging results with and without compensation by different method. (a) Without compensation. (b) Compensation with SCA. (c) Compensation with I2C method. (d) Compensation with OI4C method.

Fig. 16. Coherence coefficient image and the interferometric phase image of the imaging results of Channel 2 and Channel 4 after compensation by OI4C method.

Fig. 17. Interferometric phase images of the imaging results with different compensation method. (a) Without compensation. (b) Compensation by I2C method.

69.8, 5.6, and 126 cm from right to left in the imaging result, and the maximum position error does not exceed 1.5 cm compared with the actual layout. In addition, after compensation by the I2C method and SCA, the imaging results are also improved, although there is still some defocus.

Meanwhile, the coherence coefficient image and the interferometric phase image of the imaging results of Channel 2 and Channel 4 after compensation by OI4C method are shown in Fig. 16. It can be seen that most coherence coefficients in the target area are above 0.8, and the interferometric phases are stable after compensation, which indicates the effectiveness of the OI4C method.

In order to further demonstrate the effectiveness of the OI4C method, Fig. 17 shows the interferometric phase images of the imaging results without compensation and with compensation by the I2C method. For ease of comparison, the interferometric phase images are gated by the imaging result with compensation by the OI4C method. Compared with Fig. 16, the interferometric phases of the target area in Fig. 17 still have large fluctuations, which indicates the effectiveness of the OI4C method.

In addition, the super-resolution technology [10] can be applied to the imaging results after compensation by the OI4C method to further improve the range resolution to 4 cm. The super-resolution imaging results and the 2D slices of the first high-reflectivity strip are shown in Fig. 18.

2. Noncooperative UAV Experiment

The ISAL detection experiment of noncooperative fixed-wing UAV without artificial high-reflectivity strips (corresponding to the real scene for ISAL imaging and detection) at about 250 m distance is carried out to verify the OI4C method. The
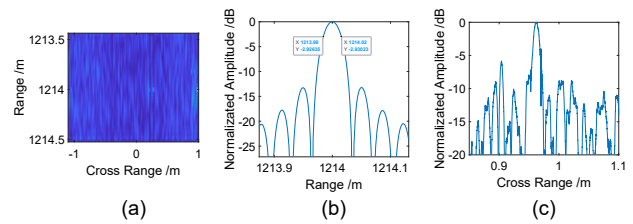
Fig. 18. Super-resolution imaging results and the 2D slices of the first high-reflectivity strip. (a) Imaging result. (b) Range slice. (c) Cross-range slice.

Table 3.   Target Parameters

Parameters	Values
Doppler center frequency	4.55 MHz
Slow time frequency modulation	282 kHz/s
Range/cross-range velocity	3.52 m/s/7.32 m/s
Squint/pitch angle	25.7°/−1.9°
Signal duration	30 ms
Doppler band vibration-caused	about 14 kHz
Cross-range imaging filter band	2.8 kHz
Target range	245.6 m

target parameters are shown in Table 3, and the unlisted system parameters are consistent with the parameters shown in Table 1.

The echo with coarse compensation in the time domain and time-frequency domain are shown in Fig. 19. Duration of the echo signal is about 30 ms, of which the high SNR signal part is only about 5 ms, which may correspond to a scattering point with high reflectivity on the fuselage, while the rest of the echo signal intensity is relatively weak.

Estimation of vibration phases is carried out by using SCA and the I2C and OI4C methods, respectively. Estimation results and time-frequency analysis after compensation by the OI4C method are shown in Fig. 20. Figure 21 displays the detection results and cross-range slices with and without the compensation by using the estimation results in Fig. 20(a), respectively. It can be seen from this that there is still some defocus with compensation by the I2C method and SCA. For the I2C method, the nonparallel of direction of the UAV and the baseline also affects estimation accuracy. By contrast, with compensation by the OI4C method, the focus degree of the results has been significantly improved, the entropy decreases from 11.63 to 9.33, the contrast increases from 0.74 to 1.08, and the cross-range resolution of the result is better than 1 cm. Subsequently, on the basis of the detection results after OI4C compensation, the PGA processing is further performed; the results show that the focus degree is slightly improved, indicating that the OI4C method
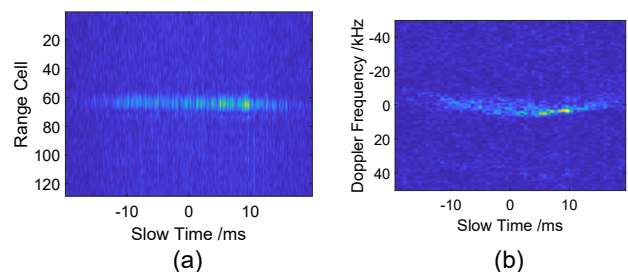
Fig. 19. Echo in (a) time domain and (b) time-frequency domain.
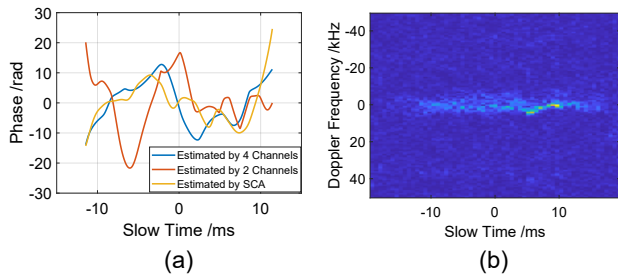
Fig. 20. (a) Estimated values of vibration phases and (b) time-frequency analysis after compensation by OI4C method.

has little estimation error. It can be seen from the processing results that it does correspond to a scattering point with high reflectivity on the fuselage of the UAV.

C. Discussion

It should be noted that the interferometry-based OI4C method needs to ensure that the interferometric phases are not wrapped, which limits the OI4C method on the Doppler band as a result of vibration in the echo when the baseline of the ladar in this paper has been determined. The vibration phases can generally be modeled as a sinusoidal function:

$$\varphi_v(t_k) = A_v \cdot \sin(2\pi \cdot F_v \cdot t_k), \qquad (9)$$

where A_v and F_v represent the amplitude and frequency of the vibration phases, respectively; then, the Doppler band caused by the vibration can be expressed as $B_v = 2|\frac{1}{2\pi}\frac{d\varphi_v(t_k)}{dt_k}| = 2A_v \cdot F_v$. It should satisfy the following equation [16]:

$$B_v < \min\left[\|\vec{V}\|/(L_{24} \cdot \cos(\theta)),\ \|\vec{V}\|/(L_{13} \cdot \sin(\theta) \cdot \sin(\phi))\right]. \qquad (10)$$

It can be seen that the slower the target velocity, the larger the phase difference between the two channels, which causes the interferometric phases to wrap more easily. As examples, for the cooperative vehicle with a velocity of 10.6 m/s, in order to ensure that the interferometric phases are not wrapped, the Doppler band caused by vibration needs to be less than 17 kHz; for the short-time signal of UAV with a velocity of 8.1 m/s, it should be less than 15 kHz. In this paper, they both met this condition. If the velocity of the target is too slow or the Doppler band is too wide, it may be considered to first reduce the Doppler band through coarse compensation and then use the OI4C method for precise vibration phases compensation.

5. CONCLUSION

While ISAL can provide high-resolution imaging results for remote sensing observations in a short time, the vibration phases of the target can cause imaging defocusing. In this paper, the orthogonal interferometry method based on time-frequency analysis is proposed to estimate and compensate the vibration phases of targets, which can effectively suppress the influence of noise on the interferometric phases, maintain the coherence of the signal, and estimate vibration phases accurately by multichannel interferometry in the inner FOV. The simulations and experiments of the cooperative vehicle at about 1200 m
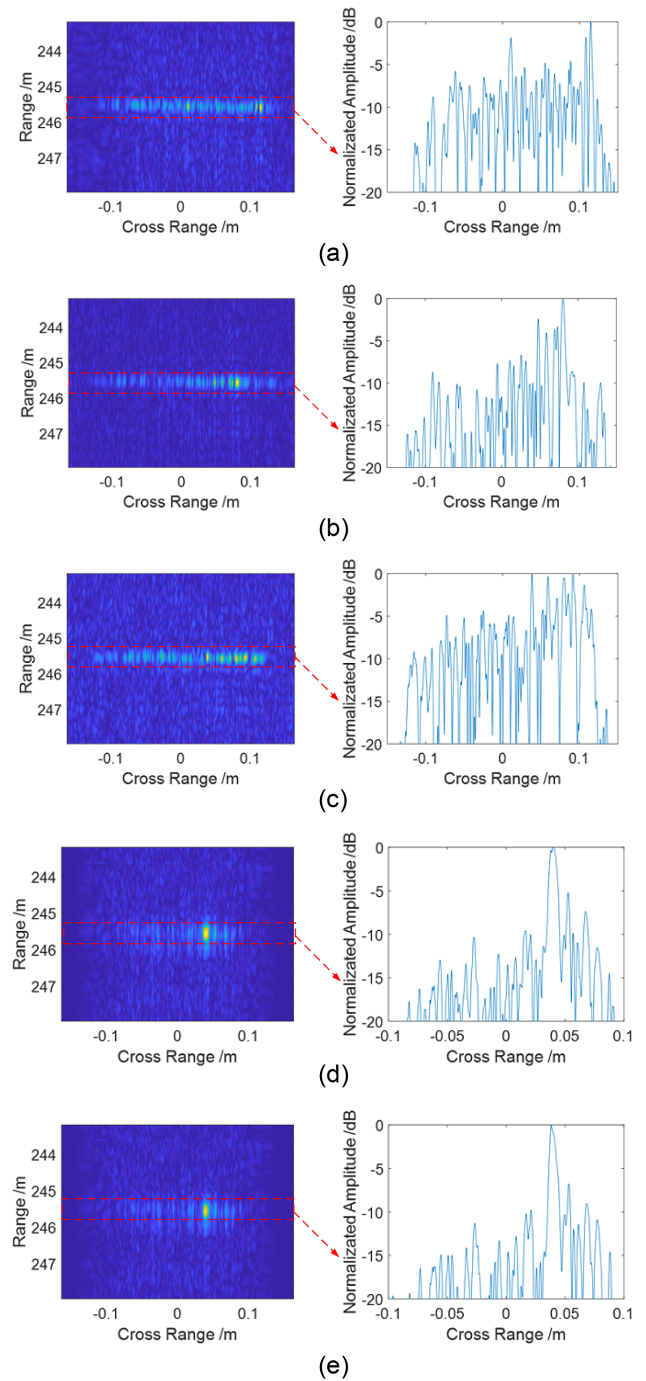
Fig. 21. Detection results with and without compensation by different method, and PGA processing. (a) Without compensation. (b) Compensation with SCA. (c) Compensation with I2C method. (d) Compensation with OI4C method. (e) PGA processing result of (d).

distance and the noncooperative UAV at about 250 m distance demonstrate the effectiveness and performance of the proposed method.

Disclosures. The authors declare no conflicts of interest.

REFERENCES

1. A. B. Gschwendtner and W. E. Keicher, "Development of coherent laser radar at Lincoln laboratory," Lincoln Lab. J. **12**, 383–394 (2000).
2. X. Hu, D. Li, and J. Du, "Image processing for GEO object with 3D rotation based on ground-based InISAL with orthogonal baselines," Appl. Opt. **58**, 3974–3985 (2019).
3. S. Wang, B. Wang, M. Xiang, X. Sun, and Y. Wu, "Synthetic aperture ladar motion compensation method based on symmetrical triangular linear frequency modulation continuous wave," Opt. Commun. **471**, 125901 (2020).
4. B. W. Krause, J. Buck, C. Ryan, D. Hwang, P. Kondratko, A. Malm, A. Gleason, and S. Ashby, "Synthetic aperture ladar flight demonstration," in *Conference on Lasers and Electro-Optics* (2011).
5. G. Cai, P. Hou, X. Ma, J. Sun, N. Zhang, G. Li, G. Zhang, and L. Liu, "The laser linewidth effect on the image quality of phase coded synthetic aperture ladar," Opt. Commun. **356**, 495–499 (2015).
6. R. S. Depoy and A. K. Shaw, "Algorithm to overcome atmospheric phase errors in SAL data," Appl. Opt. **59**, 140–150 (2020).
7. L. Guo, H. Yin, L. Yang, G. Sun, M. Xing, X. Zeng, and Y. Hu, "Sub-aperture phase error stitching for full aperture airborne SAL data processing method based on azimuth deramp," Opt. Laser Technol. **136**, 106708 (2021).
8. S. Turbide, L. Marchese, A. Bergeron, L. Desbiens, and P. Paradis, "Synthetic aperture ladar based on a MOPAW laser," Proc. SPIE **10005**, 1000502 (2016).
9. G. Zhang, J. Sun, Y. Zhou, Z. Lu, G. Li, M. Xu, B. Zhang, C. Lao, and H. He, "Ghost image in enhanced self-heterodyne synthetic aperture imaging ladar," Opt. Commun. **410**, 591–597 (2018).
10. D. Li, K. Zhou, A. Cui, M. Qiao, S. Wu, Y. Wang, Y. Yao, J. Wu, and J. Gao, "Multi-channel inverse synthetic aperture ladar imaging detection technology and experimental research," Laser Optoelectron. Prog. **58**, 1811017 (2020).
11. D. Li and X. Hu, "Optical system and detection range analysis of synthetic aperture ladar," J. Radars **7**, 263–274 (2018).
12. Z. Zhao, J. Huang, S. Wu, K. Wang, T. Bai, Z. Dai, X. Kong, and J. Wu, "Experimental demonstration of tri-aperture differential synthetic aperture ladar," Opt. Commun. **389**, 181–188 (2017).
13. Z. Song, D. Mo, N. Wang, B. Li, Y. Shao, and R. Tan, "Inverse synthetic aperture ladar autofocus imaging algorithm for micro-vibrating satellites based on two prominent points," Appl. Opt. **58**, 6775–6783 (2019).
14. X. Hu, D. Li, J. Du, M. Ma, and J. Zhou, "Vibration estimation of synthetic aperture lidar based on division of inner view field by two detectors along track," in *IEEE International Geoscience and Remote Sensing Symposium* (2016), pp. 4561–4564.
15. J. Du, D. Li, M. Ma, X. Hu, and M. Qiao, "Vibration estimation and imaging of airborne synthetic aperture lidar based on interferometry processing," Chin. J. Lasers **43**, 253–264 (2016).
16. X. Hu and D. Li, "Vibration phases estimation based on multi-channel interferometry for ISAL," Appl. Opt. **57**, 6481–6490 (2018).
17. A. Cui, D. Li, J. Wu, K. Zhou, J. Gao, M. Qiao, S. Wu, Y. Wang, and Y. Yao, "Moving target imaging of a dual-channel ISAL with binary phase shift keying signals and large squint angles," Appl. Opt. **61**, 5466–5473 (2022).
18. D. Li, X. Hu, K. Zhou, Y. Yao, and M. Qiao, "Synthetic aperture lidar imaging detection based on conformal diffractive optical system," Acta Opt. Sin. **40**, 179–192 (2021).
19. J. Gao, D. Li, K. Zhou, A. Cui, J. Wu, Y. Wang, K. Liu, S. Tan, Y. Gao, and Y. Yao, "Analysis of receiving beam broadening and detection range of lidar based on diffractive optical system," Chin. J. Lasers **50**, 0710001 (2023).
20. D. Li, J. Wu, L. Wan, D. Wang, and T. Wu, "Elementary imaging theory on space-borne synthetic aperture lidar," Acta Opt. Sin. **39**, 357–364 (2019).
21. M. Ma, "Research on moving target imaging and detection for millimeter-wave InISAR with orthorgonal baselines," Ph.D. dissertation (University of Chinese Academy of Sciences, 2017).